

Mapping Full Conformational Transition Dynamics of Intrinsically Disordered Proteins Using a Single-Molecule Nanocircuit

Dongbao Yin, Ruoyao Xiong, Zhiheng Yang, Jianfei Feng,* Wenzhe Liu, Shiyun Li, Mingyao Li, Hao Ruan, Jie Li, Lidong Li,* Luhua Lai,* and Xuefeng Guo*



Cite This: *ACS Nano* 2024, 18, 25986–25996



Read Online

ACCESS |



Metrics & More

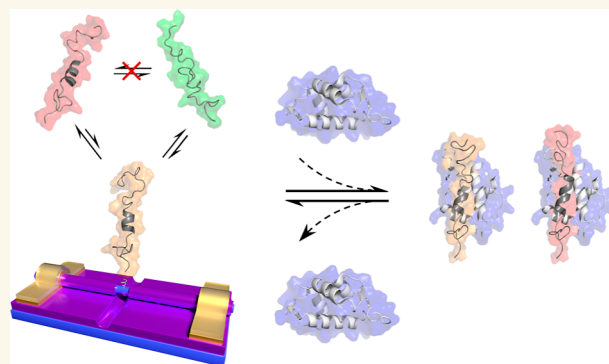


Article Recommendations



Supporting Information

ABSTRACT: Intrinsically disordered proteins (IDPs) are emerging therapeutic targets for human diseases. However, probing their transient conformations remains challenging because of conformational heterogeneity. To address this problem, we developed a biosensor using a point-functionalized silicon nanowire (SiNW) that allows for real-time sampling of single-molecule dynamics. A single IDP, N-terminal transactivation domain of tumor suppressor protein p53 (p53_{TAD1}), was covalently conjugated to the SiNW through chemical engineering, and its conformational transition dynamics was characterized as current fluctuations. Furthermore, when a globular protein ligand in solution bound to the targeted p53_{TAD1}, protein–protein interactions could be unambiguously distinguished from large-amplitude current signals. These proof-of-concept experiments enable semiquantitative, realistic characterization of the structural properties of IDPs and constitute the basis for developing a valuable tool for protein profiling and drug discovery in the future.



KEYWORDS: intrinsically disordered protein, silicon nanowire, biosensor, single-molecule dynamics, conformational transition

INTRODUCTION

Intrinsically disordered proteins (IDPs) constitute nearly a one-third of the entire protein realm and play vital roles in diverse biological phenomena.^{1–3} However, our understanding of them, notably the structural properties, falls far behind that of structured proteins. Conventional methods such as nuclear magnetic resonance (NMR) spectrometry^{4,5} and fluorescence thermal denaturation^{6,7} are instrumental in the structural and dynamics analysis of IDPs in the bulk phase. These ensemble-averaging methods, however, lack the precision required to uncover the discrete roles of the transient conformations, which are often heterogeneous in biomolecular processes. To mitigate this problem, single-molecule techniques such as high-speed atomic force microscopy (AFM),^{8,9} Förster resonance energy transfer spectroscopy,^{10–12} and nanopore sensing^{13,14} have been used in probing the transient conformations of IDPs. Nevertheless, these techniques are applicable to specific utilities considering their limitations in IDP investigation such as the tip–sample contact, unwanted external labels, or structural restrictions, emphasizing the need for further optimization.

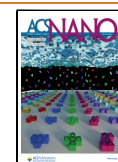
Recently, silicon nanowire field-effect transistors (SiNW–FETs) have emerged as a promising platform for ultrasensitive protein detection^{15–18} that could serve as an alternative approach to address those intractable problems in the structural and dynamics analysis of IDPs. This platform is based on the conversion of slight structural changes within the target molecules to electrical signals. This electrical conversion enables the construction of a variety of pioneering applicable platforms for single-molecule measurements.^{19–25} Label-free detection by this platform avoids viscous friction from the large label probe used for amplifying the optical signal. The intrinsic conformational transition dynamics of proteins could thus be revealed without being affected by nonuniform viscous effects. Since the conductance of the high-gain FETs is highly dependent on the local charge density,^{26,27} it allows intact

Received: March 26, 2024

Revised: August 29, 2024

Accepted: September 6, 2024

Published: September 14, 2024



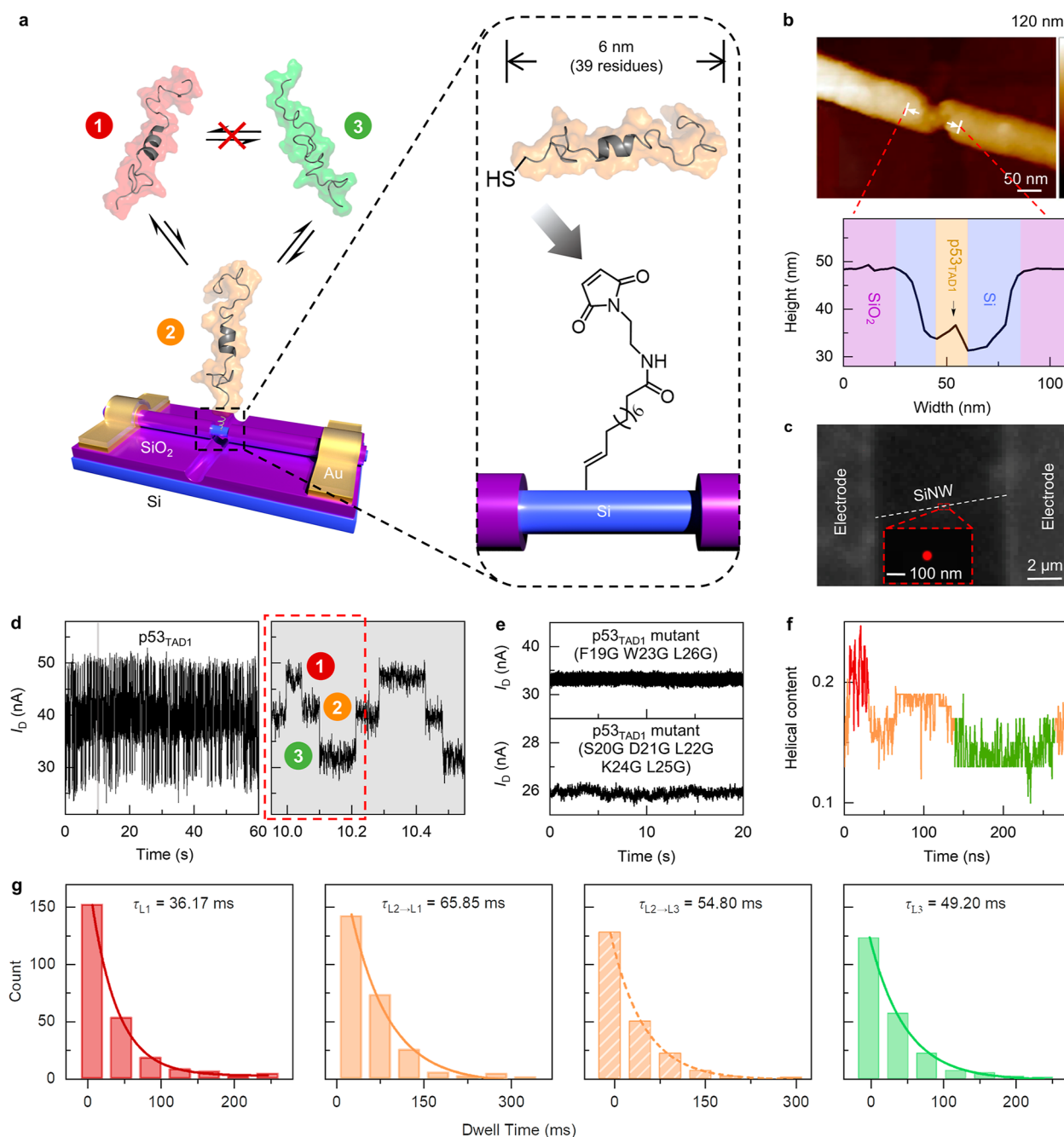


Figure 1. Device fabrication of a point-functionalized SiNW–FET biosensor and sampling transient IDP dynamics. (a) Schematic representation of a single-p53_{TAD1}-modified SiNW–FET biosensor (not to scale). The enlarged view shows the engineered p53_{TAD1} with a C-terminal cysteine for the SiNW point decoration via a thiol–maleimide Michael reaction. The nanoscale size of the silicon trench attained by chemical wet etching is comparable to that of the p53_{TAD1}. The p53_{TAD1} structure was visualized using PyMOL with PDB ID 2K8F. (b) AFM image of the silicon trench and the corresponding height profile across the trench. The small peak denotes the point decoration of p53_{TAD1} within the silicon trench. (c) Fluorescent super-resolution imaging of a 5-FAM-labeled p53_{TAD1} on the SiNW. A 490 nm laser was focused on the device, and the image was obtained after stochastic optical reconstruction. Inset: after removing the background, only one spot was obtained between metal electrodes, indicating the immobilization of a single molecule of p53_{TAD1} on the SiNW surface. (d) Real-time current recordings of p53_{TAD1} displaying a high frequency of conformational ensemble transitions (number of events: $n = 1812$, 60 s). Testing conditions: $T = 20\text{ }^{\circ}\text{C}$, $V_D = 300\text{ mV}$. Corresponding enlarged current signals display distinct steplike traces with three current levels (levels 1, 2, and 3 correspond to high, medium, and low currents, respectively). Levels 2 to 1 and 3 are reversible steps; no steps of level 1 to 3 or level 3 to 1 were observed. (e) Top: real-time current recording of a p53_{TAD1} mutant (F19G, W23G, and L26G) that lacks critical residues to form helical structures. Bottom: real-time current recording of a p53_{TAD1} mutant (S20G, D21G, L22G, K24G, and L25G) with multiple aromatic residues and disrupted helical structures. There are no obvious significant changes in current flow. (f) MD simulations of the structure trajectory of p53_{TAD1} showing the fraction of its helical content. The conformers with high, medium, and low helical contents correspond to levels 1, 2, and 3, respectively. (g) Dwell time analysis of the three current levels. Level 2 is classified into two categories according to the following levels (i.e., $\tau_{L2 \rightarrow L1}$ and $\tau_{L2 \rightarrow L3}$). Each lifetime of the transient conformation was obtained from idealized current signals by fitting to a single exponential function (number of events: $n = 243$, 243, 210, and 217, respectively).

recording of molecules with high accuracy. Liu and his co-workers²⁸ functionalized a SiNW–FET-based electrical nanocircuit with a single *c*-Myc bHLH-LZ domain allowing single-molecule-level, label-free, in situ measurements over extended periods. They successfully observed the self-folding–unfolding process of *c*-Myc and measured *c*-Myc/Max and *c*-Myc/inhibitor dissociation constants. Especially, the SiNW–FET captured a relatively stable conformation ensemble of *c*-Myc, which is important for understanding the structural characteristics and binding mechanism of IDPs.

In the present study, we used SiNW–FETs to study the structure, dynamics, and binding of p53. The tumor suppressor protein p53 comprises an N-terminal transactivation domain that contains two similar domains (TAD1 and TAD2), a DNA-binding domain, a tetramerization domain, and a C-terminal disorder domain.²⁹ Both TAD1 (residues 1–40) and TAD2 (residues 40–62) were found to be disordered in full-length p53 and when in an isolated state.^{30–32} The binding of p53_{TAD1} with mouse double minute 2 (MDM2), an E3 ligase, leads to p53 degradation in the cell. The p53_{TAD2} has an independent transcriptional activation function but interacts with different proteins, and the interaction with MDM2 is weaker. Disruption of p53 and MDM2 interaction provides opportunities for cancer treatment. Although p53_{TAD1} is perceived as an attractive therapeutic target, rational drug design remains challenging³³ due to its highly disordered structure and the conformational heterogeneity. To address this issue, we covalently conjugated a single molecule of p53_{TAD1} to a SiNW–FET and studied its conformational dynamics based on current fluctuations and their temperature dependence. We observed three major current states and attributed them to three different conformational ensembles with high to low helical contents based on the integration with temperature-dependent circular dichroism (CD) spectra, NMR spectra, and molecular dynamics (MD) simulations. We found that the helical content increased along with temperature in the range of 20–40 °C and derived the interconversion kinetics of the three states. We further introduced MDM2 to the system and directly observed its dose-dependent binding and release events to p53_{TAD1}. As only the relatively high helical-content conformations could directly bind to MDM2, it is highly possible that the binding of p53_{TAD1} with MDM2 can be described as a conformation selection process.^{34,35} This study further demonstrates that SiNW–FET technology provides an effective tool for studying the dynamic structural nature of IDPs and their interactions with other proteins in real time at the single-molecule level.

RESULTS AND DISCUSSION

Point Functionalization and Real-Time Electrical Monitoring. We first built the point-functionalized SiNW–FET and covalently conjugated a single molecule of p53_{TAD1} to the nanotrench (Figures 1a and S1). In brief, the SiNW–FET (Figure S2) was prepared using chemical vapor deposition (CVD)-grown SiNWs,³⁶ and the nanotrench was generated with electron-beam lithography. Next, the p53_{TAD1} peptide with an additional C-terminal cysteine was conjugated to the SiNW by using a functional cross-linker, harboring a maleimide (obtained from hydrosilylation and esterification) for attachment to the cysteine residue through Michael addition on the surface of the SiNW. The C-terminal cysteine has little influence on the interaction with MDM2 because the residues 19–26 serving for interaction are located at a certain distance

from the C-terminal end and connected by a flexible glycine. AFM measurements provided a height profile of approximately 6 nm across the nanotrench, in the approximate size of the fully extended p53_{TAD1}, which indicates the successful immobilization of a single protein on the SiNW (Figure 1b). This result was further confirmed by stochastic optical reconstruction microscopy images, which showed a single fluorescent spot of a fluorescein amidite-labeled p53_{TAD1} (Figure 1c).

Under a constant source-drain bias voltage (300 mV) at 20 °C, this single-molecule p53_{TAD1} functionalized SiNW–FET generated a cyclic steplike pattern with three current levels for long periods (Figure 1d), while only stable current signals were detected in control experiments of the bare devices without p53_{TAD1} modification (Figure S3). These results suggest that the current fluctuations originate from intrinsic behaviors of the modified p53_{TAD1}, which acts as a local gate and electrostatically modulates the hole carrier intensity inside the SiNW channel.¹⁵ As p53_{TAD1} is negatively charged in the PBS buffer at pH 6.8 (with a pI of 4.0), its folding makes it closer to the surface of the SiNW, thereby increasing the negative gate voltage. According to the charge transport mechanism of the p-type SiNW–FET, this would increase the hole carrier intensity and improve the conductivity of the SiNW. Therefore, we suppose that the current levels 1, 2, and 3 may correspond to three different p53_{TAD1} conformational ensembles with high, medium, and low helical contents, respectively.³⁷ Each conformational ensemble corresponds to a p53_{TAD1} residing within an energy landscape without prominent energy wells,²⁸ instead of a specific conformation because the transition between different conformations happens at a considerably rapid rate and beyond the time resolution in our experiments (~17 μs). Nevertheless, the conformational ensembles with longer dwell time are possible to be captured and characterized by different current states. In contrast, the three-level current fluctuation is absent (Figure 1e, top) on the SiNW-FET modified by a p53_{TAD1} mutant (F19G, W23G, and L26G) that lacks critical residues to form helical structures. Another possibility of the current fluctuation originating from aromatic interactions between the peptide and the SiNW has also been excluded using another p53_{TAD1} mutant (S20G D21G L22G K24G L25G) with multiple aromatic residues and disrupted helical structures (Figure 1e, bottom). These results validate that the current change of SiNW–FETs originates from the intrinsic folding of p53_{TAD1} instead of the interaction of p53_{TAD1} with the SiNW. We applied the hidden Markov model³⁸ to simulate the single-molecule behavior for the monitored three-level current fluctuations. It is noteworthy that although states 1 and 2 and 2 and 3 can interconvert, the interconversion of states 1 and 3 can only be realized via state 2. To further analyze the possible conformational states, we performed all-atom MD simulations to sample the p53_{TAD1} conformations and analyze the helical content (Figure 1f). The MD trajectories indicated that residues 6–29 took interchangeable disordered and partially helical conformations. In a typical MD simulation, direct conformational clustering based on the helical content gave three clusters in general, matching the three-level current fluctuations (indicated by the red dashed line in Figure 1d) that were experimentally measured for the single molecule of p53_{TAD1}. In another previous study of p53_{TAD1} conformation sampling, the MD results for different initial conformations of p53_{TAD1} over a time period totaling 900 ns are similar.³⁷

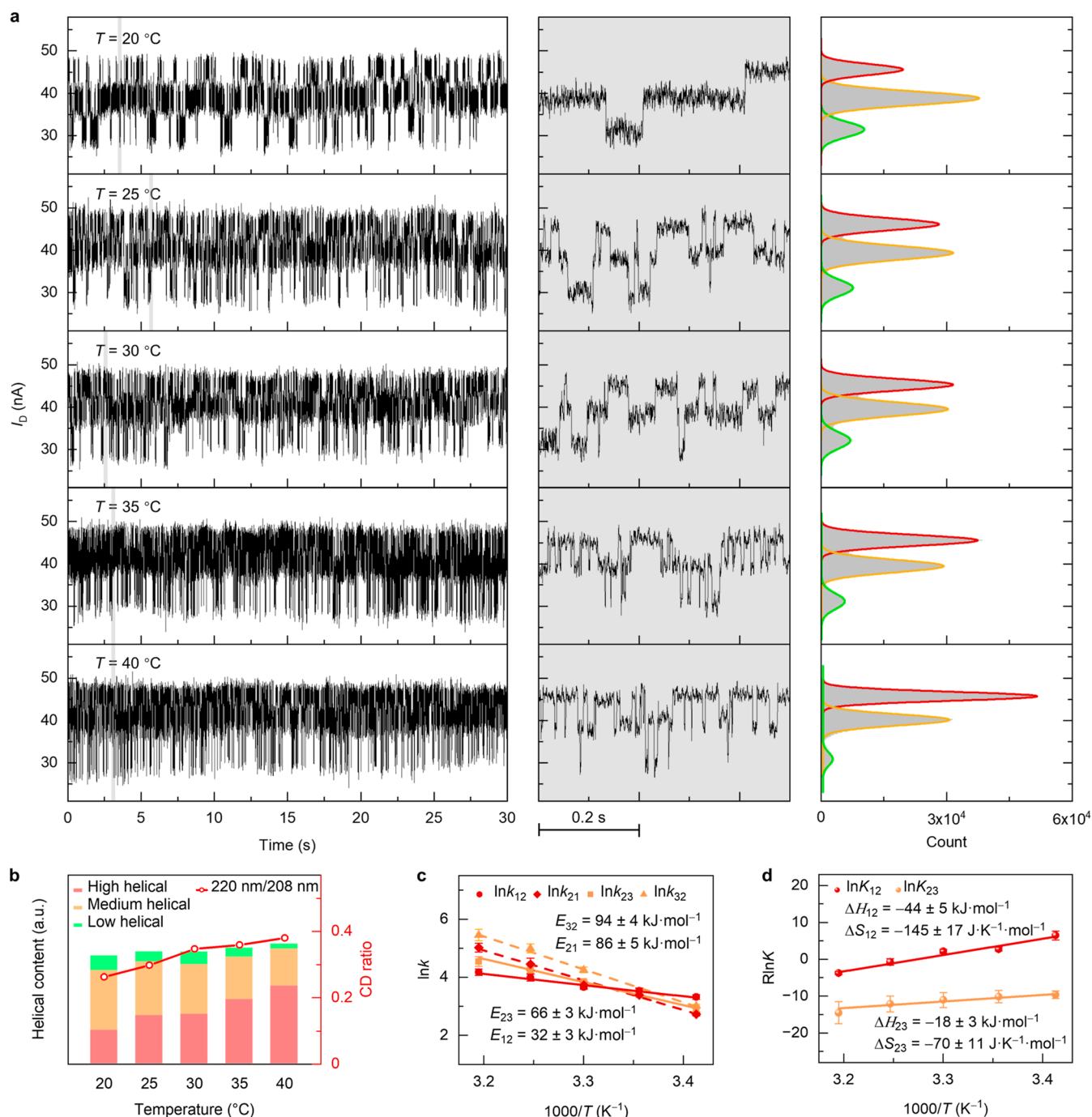


Figure 2. Dynamic characterization of a single molecule of p53_{TAD1}. (a) Real-time current recordings of a single molecule of p53_{TAD1} at various temperatures ranging from 20 to 40 °C. Corresponding enlarged current signals and histograms display distinct steplike traces with three current levels. Testing condition: $V_D = 300$ mV. (b) Histogram of the helical content of p53_{TAD1} versus the temperature. The proportion of level 1 (high helical conformers, red bars), level 2 (medium helical conformers, orange bars), and level 3 (low helical conformers, green bars) gives relative contributions of $\sim 23\%$, $\sim 18\%$, and $\sim 15\%$ based on MD, respectively. Data from CD measurements in bulk solution are shown as a red line. The CD spectra of p53_{TAD1} are shown in Figure S7. (c) Arrhenius plots of the forward and reverse disorder–helix transitions between the characterized conformers. The activation energies of the forward (E_{32} and E_{21}) and reverse (E_{12} and E_{23}) transitions were obtained by linear fits of the rate constants at various temperatures using the Arrhenius equation. (d) Enthalpy–entropy compensation of conformational ensemble transitions. The apparent enthalpies (ΔH_{12} and ΔH_{23}) and entropies (ΔS_{12} and ΔS_{23}) were obtained by linear fits of plots of $R \ln K$ versus $1000/T$ according to the thermodynamic relation.

Although there is a time scale difference between the MD and the current signals, it is necessary to consider the limitations of force fields used in MD simulations and the electric field applied to the p53_{TAD1} on the SiNW–FETs, which plays a role in stabilizing conformational ensembles. Furthermore, we

idealized the current fluctuations using QuB software (Figure S5) and measured the dwell times in each current level (Figure 1g). The dwell time in level 2 is classified into two categories according to its following levels (level 2 to 1 and level 2 to 3). The data were well fitted to single exponential functions to

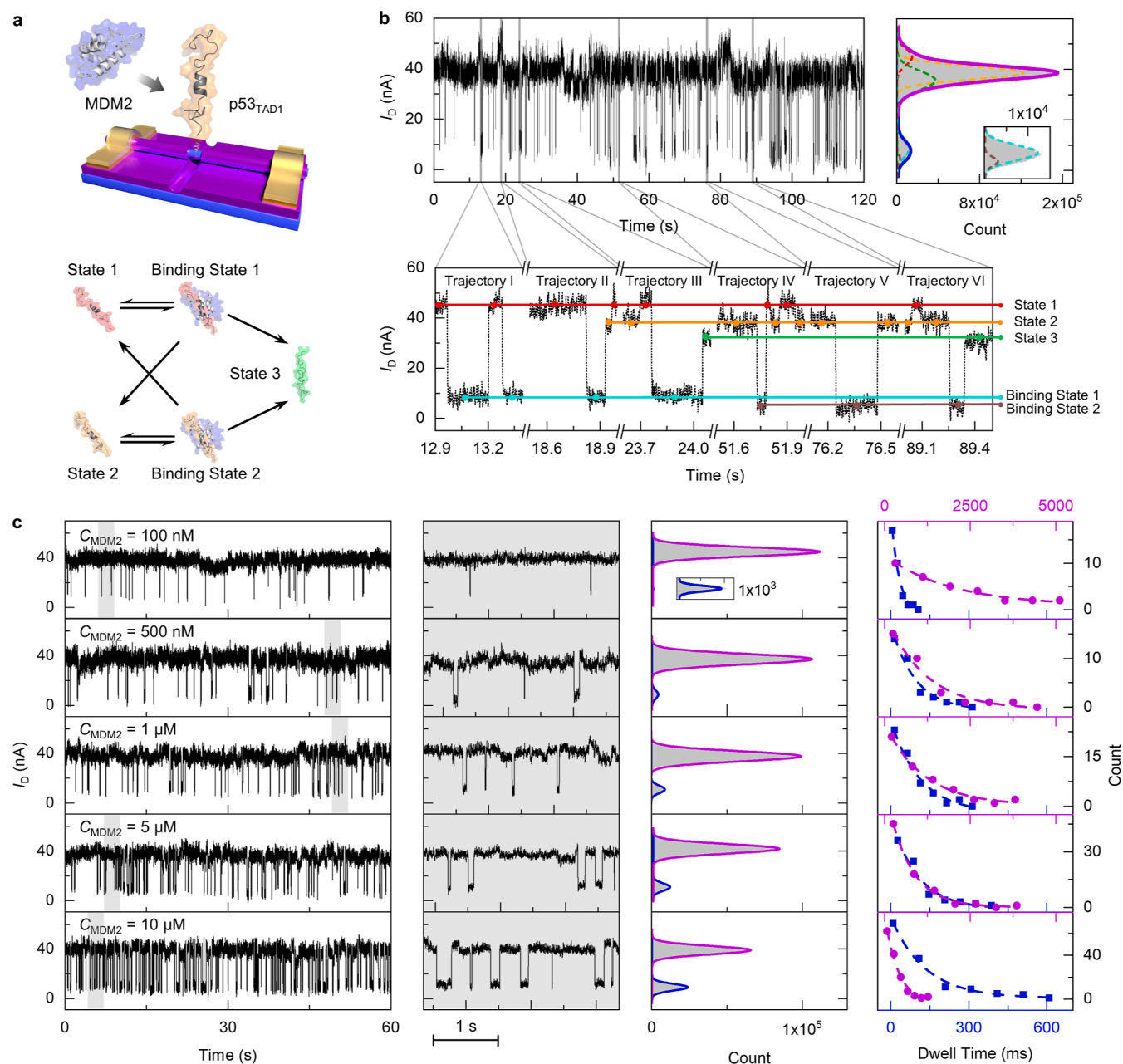


Figure 3. Measurements of transient protein–protein interactions (PPIs) between p53_{TAD1} and MDM2. (a) Top: schematic representation of a single-p53_{TAD1}-modified SiNW–FET biosensor for the real-time measurement of transient PPIs with MDM2 (not to scale). The MDM2 structure was visualized using PyMOL with PDB ID, 2K8F. Bottom: schematic representation of MD trajectories of PPIs between p53_{TAD1} and MDM2. p53_{TAD1}–MDM2 binding events occur only when p53_{TAD1} attains sufficiently high helical contents (states 1 and 2). (b) Real-time current recordings of transient PPIs and corresponding histograms displaying MD trajectories. The distributions of the well-characterized three unbound states (i.e., p53_{TAD1} conformational ensemble transitions) are indicated by red, orange, and green, respectively; the distributions of two new states (i.e., MDM2-bound states) are indicated by sky blue and brown, respectively. Corresponding enlarged current signals display six types of MD trajectories, i.e., trajectory I: state 1 → binding state 1 → state 1; trajectory II: state 1 → binding state 1 → state 2; trajectory III: state 1 → binding state 1 → state 3; trajectory IV: state 2 → binding state 2 → state 1; trajectory V: state 2 → binding state 2 → state 2; and trajectory VI: state 2 → binding state 2 → state 3. (c) Real-time current recordings of transient PPIs at various MDM2 concentrations ranging from 100 nM to 10 μM. The distributions of the three unbound states (τ_d) and the two MDM2-bound states (τ_b) are combined and plotted as dashed lines, respectively, in the histograms. The dwell times of the combined unbound states and the MDM2-bound states were fitted to single exponential functions, respectively. The dependence of τ_d and τ_b on the MDM2 concentration is illustrated in Table S4. Testing conditions: $T = 25\text{ }^\circ\text{C}$, $V_D = 300\text{ mV}$.

gain the lifetime (τ) of each level, suggesting a single-barrier transition of the free-energy landscapes of these conformations. Conformational ensemble transition rates (k), the reciprocal of their corresponding lifetimes, were also calculated and are listed in Table S2.

Conformational Transition Dynamics of p53_{TAD1}. Next, we performed temperature-dependent electrical recordings to extrapolate the enthalpic and entropic contributions to the dynamic rate constants of the p53_{TAD1} conformational ensemble transitions (Figure 2a). We found that the

distribution of the conformational states is temperature-dependent. In the temperature range from 20 to 40 °C, the proportion of state 1 increases from $26 \pm 3.6\%$ to $57 \pm 1.2\%$, while the proportion of states 2 and 3 decreases from $56 \pm 2.1\%$ to $36 \pm 1.5\%$ and from $18 \pm 2.1\%$ to $6.3 \pm 2.5\%$, respectively (Table S3). Although absolute values of the current levels varied from read to read among different SiNW-FET devices, the current patterns and the temperature dependence were highly reproducible (Figure S6). This temperature dependence looks contrary to the general impression that heating destroys the protein secondary structure; however, it was demonstrated by CD and NMR experiments. We further used CD to analyze the secondary structures of p53_{TAD1} and their temperature dependence changes in solution (Figure S7). The helical structures have negative peaks at 220 and 208 nm, and therefore, the ratio of absorbance values at 220 and 208 nm was used to evaluate the helical rate of p53_{TAD1}. This ratio shows a consistent tendency with the helical content estimated by single-molecule p53_{TAD1} functionalized SiNW-FETs (Figure 2b). The helical content at each temperature was also estimated using BeStSel, a Web server for predicting secondary structures via protein CD spectroscopy.³⁹ The BeStSel estimated results as shown in Table S1 also reveal increased helical contents with increasing temperature. This temperature dependence was also supported by the increase of average C_α chemical shifts of p53_{TAD1} in NMR study (Figure S7c,d). Average α -carbon chemical shifts at 20, 25, 30, 35, and 40 °C are 59.099, 59.138, 59.194, 59.219, and 59.281, respectively. As C_α chemical shifts are indicative of the secondary structure of proteins, an increased C_α chemical shift suggests an increase in helical contents with increasing temperature.⁴⁰ The results of CD and NMR experiments are consistent with MD: most of the p53_{TAD1} is a random coil with a small amount of helices. When the temperature rises, some of the disordered structures will undergo helical transformation, and the part with the most obvious nuclear magnetic shift is not the residue with a higher tendency to helix originally (F19 to L26) but the disordered structures. Based on these analyses, we can conclude that current levels 1 to 3 correspond to conformational states with high to low helical contents.

We further carried out quantitative analysis. The temperature-dependent dynamics data were plotted as $\ln k$ versus $1000/T$, and an Arrhenius fitting to the data gives positive activation energies of the forward and reverse disorder-helix transitions in the three characterized conformations (E_{32} , E_{23} , E_{21} , and E_{12}) (Figure 2c). The Arrhenius dynamics illustrates an accelerating effect of temperature on the conformational ensemble transitions of p53_{TAD1}, which is observed for structural changes of peptides (e.g., helix formation) in solution.^{41,42} The equilibrium constants of the conformational ensemble transition dynamics (K_{12} and K_{23}) in the temperature gradients were also calculated and are listed in Table S3. To gain fundamental insights into the forces that drive protein conformational ensemble transitions, further thermodynamic analysis was performed. Conformational ensemble transitions were cast into the Gibbs free energy to extract the apparent enthalpies (ΔH_{12} and ΔH_{23}) and entropies (ΔS_{12} and ΔS_{23}) from plots of $R \ln K$ versus $1000/T$, as shown by linear fittings to the data (Figure 2d). It is noteworthy that the transition free energy ΔG_{12} of p53_{TAD1} conformations with high helical content to medium helical content decreases to below zero at ~ 34 °C ($1000/T = 3.26$) (Figure S8), which indicates a transition from spontaneous to nonspontaneous processes, i.e.,

the high helical conformation predominates above ~ 34 °C, while the medium helical conformation predominates below that temperature.

Interaction Trajectories of p53_{TAD1}-MDM2. Although IDPs dynamically sample a multitude of conformational states when present alone in solution, many of them undergo conformational ensemble transitions to ordered forms upon binding to their biological targets, in a mechanism known as coupled binding and folding.⁴³ We next investigated the binding mechanism of p53_{TAD1} and MDM2⁴⁴ (detailed protein information is shown in Figures S9 and S10).

After addition of 1 μ M MDM2 to the single-p53_{TAD1}-modified SiNW-FET device, two additional low-current fluctuation levels (~ 8 nA) appeared (Figure 3a,b) in addition to the original current fluctuation levels 1 to 3. Control experiments of the bare devices without p53_{TAD1} modification excluded the possibility that these new current signals originated from the interaction between MDM2 and the device (Figure S11). As MDM2 is positively charged in the PBS buffer at pH 6.8 (pI 9.0), a positive gate voltage will be applied when MDM2 binds to the immobilized p53_{TAD1} on the surface of the SiNW, which would cause the conductance of the p-type SiNW-FETs to decrease to low levels. The dissociation of MDM2 withdrew the positive gate voltage, and the conductance of the SiNW-FETs would recover to high levels. It is noted that in Figure 3b, the current difference between binding state 1 and binding state 2 is smaller than that between state 1 and state 2. These current differences reveal the fact that the MDM2 bound to a high helical p53_{TAD1} locates closer to the SiNW than that bound to a medium helical p53_{TAD1}. This finding is understandable because a high helical content tends to make p53_{TAD1} closer to the SiNW. Therefore, MDM2 bound to state 1 generates a more significant reduction of the current level, resulting in a smaller current difference between binding state 1 and binding state 2.

MDM2 is capable of binding to the F19 to L26 residue α helix in the folded structure of p53_{TAD1}, and the binding events occur only when p53_{TAD1} attains sufficiently high helical contents.^{45,46} This helix-dependent binding can be demonstrated by a p53_{TAD1} mutant (S20G D21G L22G K24G L25G)-modified SiNW-FET, where the current fluctuation of binding events is invisible (Figure S4) because of the absence of helical structures. Therefore, the two low-current fluctuation levels should represent the p53_{TAD1}-MDM2 complexes with p53_{TAD1} attaining high and medium helical contents, respectively (binding states 1 and 2) (Figure 3a, bottom). Accordingly, six types of binding and dissociation trajectories were defined (Figure 3a,b). In trajectory I, p53_{TAD1} with the high helical content (state 1) binds to MDM2 forming a p53_{TAD1}-MDM2 complex (binding state 1) and then dissociates. In trajectories II and III, p53_{TAD1} with the high helical content (state 1) binds to MDM2 (binding state 1), dissociates, and unfolds to the conformers with medium (state 2) or low helical contents (state 3), respectively. In trajectories IV, V, and VI, p53_{TAD1} with the medium helical content (state 2) binds to MDM2 (binding state 2), dissociates, and transforms to the conformers with high (state 1), medium (state 2), or low helical contents (state 3), respectively. These findings suggest that p53_{TAD1} interacts with MDM2 in different binding and dissociation modes. Among the three conformational states of unbound p53_{TAD1}, only states 1 and 2 are likely to transform to binding states due to their relatively high helical contents to form a stable complex with MDM2. In

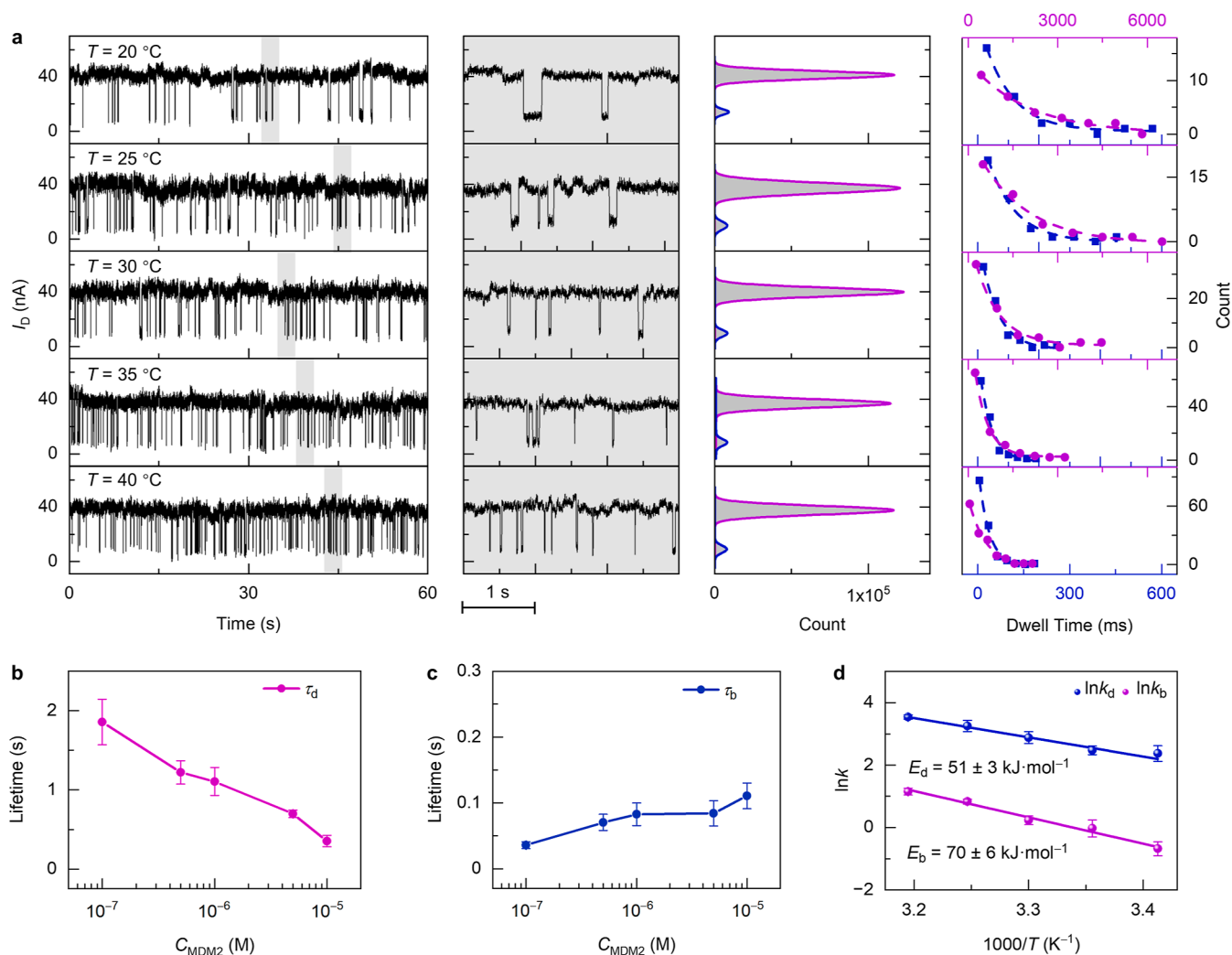


Figure 4. Dynamic characterization of transient PPIs between p53_{TAD1} and MDM2. (a) Real-time current recordings of transient PPIs at various temperatures ranging from 20 to 40 °C. Corresponding enlarged current signals and histograms display distinct steplike traces associated with unbound states and MDM2-bound states. The distributions of the unbound states and the MDM2-bound states are combined and plotted as dashed lines, respectively, in the histograms. The dwell times of the combined unbound states and the MDM2-bound states were fitted to single exponential functions, respectively. The dependence of τ_d and τ_b on temperature is illustrated in Table S5. Testing conditions: $C_{\text{MDM2}} = 1 \mu\text{M}$, $V_D = 300 \text{ mV}$. (b,c) Lifetimes of unbound states (purple) and MDM2-bound states (blue) at five different MDM2 concentrations varying from 10^{-7} to 10^{-5} M (Figure 3c). Error bars were calculated from the current data of three different devices. (d) Arrhenius plots of the forward and reverse disorder–helix transitions between the characterized conformers. The activation energies of the binding (E_b) and dissociation (E_d) processes were obtained by linear fits of the rate constants at various temperatures using the Arrhenius equation.

contrast, conformational state 3 that lacks the helical structure cannot bind to MDM2 before converting to conformational states 1 or 2. Upon dissociation, p53_{TAD1} may retain its original conformational state as in the complex or transform into one of the other two conformations due to its intrinsically disordered nature. Overall, our findings contribute to the understanding of the regulatory mechanism of MDM2 on p53 degradation and transcriptional activity.^{47–49}

Binding and Dissociation Dynamics of p53_{TAD1}–MDM2. The single-molecule dynamics of the interaction dependent on the MDM2 concentration (Figure 3c) and temperature (Figure 4a) were also investigated. We found that the frequency of the binding events became higher along with the increase of MDM2 concentrations. The dynamic process of p53_{TAD1}–MDM2 interaction is simplified to a two-step binding and dissociation, where states 1, 2, and 3 are considered as an unbound state and binding states 1 and 2

are considered as a bound state. Therefore, the current signals of the p53_{TAD1}–MDM2 interaction can be regarded as a two-level fluctuation characterized by two Gaussian peaks (purple and blue in the histogram of Figure 3b). The histograms of dwell times (right panels in Figures 3c and 4a) were fitted to single exponential functions to evaluate the lifetimes of the unbound state (τ_d) and the bound state (τ_b). As shown in Figure 4b,c, when the MDM2 concentration increases from 100 nM to 10 μM , τ_d exhibits a significant variation of 1.5 s in comparison with τ_b , which changes by only 0.07 s. The substantial variation of τ_d can be attributed to the shift in the chemical equilibrium by the changed MDM2 concentrations. The increased concentration of MDM2 can shift the chemical equilibrium toward the formation of the p53_{TAD1}–MDM2 complex, thereby leading to a significantly decreased τ_d . The nonlinear decrease in τ_d with increasing MDM2 concentrations may be explained by the dynamic conformational ensemble

transition involved in τ_d . Within various conformational ensembles of p53_{TAD1}, only high or medium helical contents are capable of rebinding to MDM2. The distribution of helical contents is likely different with the variation of MDM2 concentration. This dynamic behavior adds complexity to the binding kinetics, leading to a nonlinear relationship between the τ_d and MDM2 concentration. In addition, it is possible that the local environment around the single immobilized p53_{TAD1} differs from the bulk concentration in solution at high MDM2 concentrations, potentially contributing to the observed nonlinearity. Nevertheless, this concentration variation only has a limited effect on the dissociation process of the p53_{TAD1}–MDM2 complex, thus τ_b shows relatively stable values. Considering the induced-fit mechanism of PPIs⁵⁰ that the protein tends to transit into tightly bound conformations after the contact with the partner, a higher MDM2 concentration is possible to induce increased helical contents in each conformational ensemble of p53_{TAD1}. The hydrophobic interaction between p53_{TAD1} and MDM2 may be enhanced by the increased helical contents, leading to a more stable complex structure, which slightly increased the lifetime of the bound state with increasing MDM2 concentrations in Figure 4c.

Temperature-dependent current recordings were then carried out to analyze the dynamic behaviors between p53_{TAD1} and MDM2 (Figure 4a). Despite the two conductance histograms showing two similar Gaussian distributions at different temperatures, the frequency of current fluctuations increased with rising temperature. By fitting the dwell time histogram (right panel in Figure 4a) to single exponential functions, τ_d and τ_b at each temperature can be determined. Figure 4d shows the temperature-dependent binding rate (k_b) and dissociation rate (k_d) evaluated using $k = 1/\tau$. Both k_b and k_d were positively correlated with the temperature. This is consistent with our common understanding of the relationship between chemical reaction rates and temperature. These temperature-dependent experimental results also could be plotted as $\ln k$ versus $1000/T$ and the linear fittings according to the Arrhenius equation (Figure 4d) afforded the activation energies of the binding ($E_b = 70 \pm 6 \text{ kJ}\cdot\text{mol}^{-1}$) and dissociation ($E_d = 51 \pm 3 \text{ kJ}\cdot\text{mol}^{-1}$) processes. E_b and E_d represent the minimum energy barriers required for MDM2 to bind to high or medium helical p53_{TAD1} and for MDM2 to dissociate from p53_{TAD1}, respectively. A higher apparent E_b indicated that IDPs exhibit a mechanism of partner binding and dissociation that involves a higher energy barrier for the binding process. This could be attributed to certain IDPs, like p53 in the study, that require specific prebinding conformations, such as a helical conformation for effective binding. It was reported that increasing helical conformation content by mutating Pro27 to Ala in p53_{TAD1} (Figure S12) can enhance the binding affinity between p53_{TAD1} and MDM2.⁵¹ We also studied the dynamic behavior of this p53_{TAD1} mutant. The corresponding dynamic results have been shown in Table S6, where the k_b of p53_{TAD1} mutant is 4.2 times higher than that of the wild-type p53_{TAD1}. In contrast, the k_d of them are nearly the same, resulting in a smaller K_D for the p53_{TAD1} mutant. Therefore, a stronger binding affinity of the p53_{TAD1} mutant induced by increased helical contents has been confirmed, consistent with previous studies in bulk solution.⁵¹

CONCLUSIONS

We developed a point-functionalized SiNW–FET biosensor for real-time sampling of the p53 dynamic conformational ensemble at single-molecule resolution. We identified three-level current fluctuations for p53_{TAD1} and their temperature-dependent interconversions. Through integrated analysis with the temperature-dependent ensemble CD and NMR studies, the three levels of currents from high to low can be assigned as three conformational states with high, medium, and low helical contents. Only the two conformational states with relatively high helical contents can bind to MDM2 directly, and the conformational state with low helical content needs to change to the higher helical conformations for binding. Our study demonstrates that MDM2 selects suitable p53_{TAD1} conformations to bind, which then reshape the conformational ensemble of p53_{TAD1}.

Due to the conformational heterogeneity of IDPs, the structure and functions of these molecules are often quite different from the average. Conventional ensemble experiments may not provide sufficient information to understand the structure and function relationship. Single-molecule-level studies can uncover distinct conformational states and their interconversion dynamics, which are crucial for understanding IDP functions. Our study shows that combining single-molecule detection using the SiNW–FET biosensor with ensemble experimental studies and simulations can reveal the detailed conformational interconversions and dynamic binding processes, which can generally be applied in IDP dynamic structure and interaction investigations. Our results also suggest that designing molecules to bind and stabilize p53_{TAD1} or other IDPs in nonbinding conformations provides a promising strategy for IDP binder design as exemplified in our previous study.³⁷

MATERIALS AND METHODS

Device Fabrication and Protein Connection. Similar to the previous method,^{15–18} SiNWs were grown on a 3 mm × 5 mm silicon wafer. Gold nanoparticles with a 20 nm diameter were deposited on the wafer as catalysts for CVD. 1.8 sccm disilane as the reactant source, 0.35 sccm diborane as the p-type dopant, and 6.0 sccm H₂ as the carrier gas were used to synthesize boron-doped p-type SiNWs. After that, SiNWs were transferred to a 15 mm × 17 mm silicon wafer with a 1000 nm-thick oxide layer through direct mechano-sliding transfer.²⁷ Layers of 8 nm Cr followed by 80 nm Au were deposited to form metal electrodes through thermal evaporation. 60 nm SiO₂ was then deposited through electron beam thermal evaporation to form a protective layer preventing leakage into the solution phase. A 10 nm-wide line pattern was introduced to the prepared SiNW transistor by high-resolution electron beam lithography and a buffered HF solution was used to etch SiO₂ on the SiNW surface in the pattern. Subsequently, we added 3 mg of undecyonic acid to the fresh-etched device. The reaction was performed for 10 h under argon conditions, and then, the device was soaked in dichloromethane for 10 min to remove remaining reactants. After that, the device was immersed in PBS (pH = 6.5) of 20 mM *N*-hydroxysuccinimide and 10 mM 1-ethyl-3-[3-(dimethylamino)propyl] carbodiimide. The reaction was performed for 2 h, and then, the device was rinsed with deionized water. Then, a dimethylformamide solution of 10 mM 1-(2-aminoethyl)maleimide hydrochloride was added to the device under an argon atmosphere for 2 h to achieve a maleimide-functionalized terminal. After that, 50 μL of PBS of 10 μM p53_{TAD1} with the Cys terminal was dropped on the devices for 12 h at 4 °C for protein connection, followed by a rinsing process with PBS for 5 min.

Electrical Characterization. The I – V curves were measured by an Agilent B1500A semiconductor parameter system and a Karl Suss

(PMS) manual probe station. The $I-t$ curves were sampled by the HF2LI lock-in amplifier at 300 mV bias and 5 kHz bandwidth. The current signals were amplified by a DL1211 amplifier and then recorded by a high-speed acquisition card from NIDAQ at a rate of 28,800 samples per second. An INSTEC hot/cold chuck with a proportion–integration–differentiation (PID) control system and liquid nitrogen cooling system has an accuracy of 0.001 °C and was placed under the device to regulate the test temperature. The temperature was stabilized by the PID control system for 20 min after each temperature adjustment. The solution environment during electrical characterizations was provided by a PDMS microchamber with a hole of ≈ 2 mm as a reaction chamber covered on the device surface. 50 μ L of PBS with a specific concentration was then dropped into the microchamber.

Optical Characterization. 5-FAM was used as the fluorescence group on p53_{TAD1} for the fluorescence characterization. A stochastic optical reconstruction microscope (Nikon Ni-E) with a $\times 100$ objective lens was positioned in close contact with a ~ 100 μ m-thick homemade polydimethylsiloxane microchannel on the device through the lens oil. The device was excited by a 490 nm laser with an EMCCD (Andor) used to receive the feedback emitted light and the fluorescence spectra. The reconstruction and analysis of the pictures used the Advanced Research software.

MD Simulations. The conformation of the p53 1–39 peptide (p53_{TAD1}) within the p300 Taz1–p53_{TAD1} structure (PBD ID, 2K8F) was used as the starting structure and the peptide termini were amidated.⁵² To explore suitable force fields for p53_{TAD1}, all-atom MD simulations were conducted with the GROMACS 5.0.7 package.⁵³ The RSFF2+ force field with the TIP4P-D water model was used.^{54,55} The initial structure was also from the p300 Taz1–p53_{TAD1} structure with termini amidated. Electrostatics were treated using the PME method and van der Waals interactions were cut off at 10 Å. All bonds involving hydrogen were restrained using LINCS.^{51,56}

CD Spectra. CD spectra were recorded using a 1 mm-path-length quartz cuvette at 25 °C or from 20 to 40 °C, on a BioLogic MOS-450 AF/AF-CD spectropolarimeter with Peltier TCU-250.^{57,58}

NMR Spectra. The ¹³C HSQC experiments were recorded on a Bruker AVANCE III HD 950 MHz spectrometer equipped with a cryoprobe from 20 to 40 °C. All the spectra were recorded with 512 \times 100 complex points, and the spectral width was 11398 Hz in the 1H dimension (w_1) and 15279 Hz in the ¹³C dimension (w_2) centered at 40 ppm. A relaxation delay of 1.1 s was used; the number of scans was 64. NMR samples contained 1 mM p53_{TAD1} peptide in 50 mM Na phosphate, pH 6.8, 150 mM NaCl, 90% H₂O, 10% D₂O.

ASSOCIATED CONTENT

Supporting Information

The Supporting Information is available free of charge at <https://pubs.acs.org/doi/10.1021/acsnano.4c04064>.

Peptide and protein information; device fabrication and characterization; MD simulations and analysis; real-time current measurement and dynamics analysis; CD spectra and NMR spectra; thermodynamic analysis; MDM2 expression, purification, and characterization; isothermal titration calorimetry data collection and analysis; real-time current measurement in MDM2 solution; real-time current measurement of the p53_{TAD1} mutant; and detailed dynamic results (PDF)

AUTHOR INFORMATION

Corresponding Authors

Jianfei Feng – Beijing National Laboratory for Molecular Sciences, College of Chemistry and Molecular Engineering, Peking University, Beijing 100871, P. R. China; [orcid.org/0000-0002-5399-8973](mailto:jffeng@pku.edu.cn); Email: jffeng@pku.edu.cn

Lidong Li – State Key Laboratory for Advanced Metals and Materials, School of Materials Science and Engineering, University of Science and Technology Beijing, Beijing 100083, P. R. China; [orcid.org/0000-0003-0797-2518](mailto:lidong@mater.ustb.edu.cn); Email: lidong@mater.ustb.edu.cn

Luhua Lai – Beijing National Laboratory for Molecular Sciences, College of Chemistry and Molecular Engineering, Peking University, Beijing 100871, P. R. China; Peking-Tsinghua Center for Life Sciences and Center for Quantitative Biology, Academy for Advanced Interdisciplinary Studies, Peking University, Beijing 100871, P. R. China; [orcid.org/0000-0002-8343-7587](mailto:lh lai@pku.edu.cn); Email: lh lai@pku.edu.cn

Xuefeng Guo – Beijing National Laboratory for Molecular Sciences, College of Chemistry and Molecular Engineering, Peking University, Beijing 100871, P. R. China; Center of Single-Molecule Sciences, College of Electronic Information and Optical Engineering, Nankai University, Tianjin 300350, P. R. China; National Biomedical Imaging Center, Peking University, Beijing 100871, P. R. China; [orcid.org/0000-0001-5723-8528](mailto:guoxf@pku.edu.cn); Email: guoxf@pku.edu.cn

Authors

Dongbao Yin – Beijing National Laboratory for Molecular Sciences, College of Chemistry and Molecular Engineering, Peking University, Beijing 100871, P. R. China; State Key Laboratory for Advanced Metals and Materials, School of Materials Science and Engineering, University of Science and Technology Beijing, Beijing 100083, P. R. China; [orcid.org/0009-0003-4700-085X](mailto:yindb@pku.edu.cn)

Ruoyao Xiong – Beijing National Laboratory for Molecular Sciences, College of Chemistry and Molecular Engineering, Peking University, Beijing 100871, P. R. China

Zhiheng Yang – Beijing National Laboratory for Molecular Sciences, College of Chemistry and Molecular Engineering, Peking University, Beijing 100871, P. R. China; State Key Laboratory for Advanced Metals and Materials, School of Materials Science and Engineering, University of Science and Technology Beijing, Beijing 100083, P. R. China

Wenzhe Liu – Beijing National Laboratory for Molecular Sciences, College of Chemistry and Molecular Engineering, Peking University, Beijing 100871, P. R. China

Shiyun Li – Beijing National Laboratory for Molecular Sciences, College of Chemistry and Molecular Engineering, Peking University, Beijing 100871, P. R. China

Mingyao Li – Beijing National Laboratory for Molecular Sciences, College of Chemistry and Molecular Engineering, Peking University, Beijing 100871, P. R. China

Hao Ruan – Beijing National Laboratory for Molecular Sciences, College of Chemistry and Molecular Engineering, Peking University, Beijing 100871, P. R. China

Jie Li – Beijing National Laboratory for Molecular Sciences, College of Chemistry and Molecular Engineering, Peking University, Beijing 100871, P. R. China

Complete contact information is available at:

<https://pubs.acs.org/doi/10.1021/acsnano.4c04064>

Author Contributions

D.Y., R.X., and Z.Y. contributed equally to this work. X.G., L.Lai, and L.Li conceived and designed the experiments. D.Y., Z.Y., and J. F. fabricated the devices and performed the device measurements, with contributions from W. L., Z.Y., S.L., M.L., and J.L. R.X. and H.R. prepared the protein samples and

performed MD simulations and NMR and CD experiments. D.Y., J.F., R.X., X.G., and L.Lai analyzed the data and wrote the paper. All the authors discussed the results and commented on the manuscript.

Notes

The authors declare no competing financial interest.

ACKNOWLEDGMENTS

We acknowledge primary financial supports from the National Key R&D Program of China (2021YFA1200101 and 2022YFE0128700), the National Natural Science Foundation of China (22150013, 21727806, 21933001, and 21633001), Beijing National Laboratory for Molecular Sciences (BNLMS-CXXM-202407), and the Natural Science Foundation of Beijing (2222009).

REFERENCES

- (1) Wright, P. E.; Dyson, H. J. Intrinsically unstructured proteins: re-assessing the protein structure-function paradigm. *J. Mol. Biol.* **1999**, *293* (2), 321–331.
- (2) Oates, M. E.; Romero, P.; Ishida, T.; Ghalwash, M.; Mizianty, M. J.; Xue, B.; Dosztanyi, Z.; Uversky, V. N.; Obradovic, Z.; Kurgan, L.; Dunker, A. K.; Gough, J. D2P2: database of disordered protein predictions. *Nucleic Acids Res.* **2012**, *41* (D1), D508–D516.
- (3) Wright, P. E.; Dyson, H. J. Intrinsically disordered proteins in cellular signalling and regulation. *Nat. Rev. Mol. Cell Biol.* **2015**, *16* (1), 18–29.
- (4) Gibbs, E. B.; Cook, E. C.; Showalter, S. A. Application of NMR to studies of intrinsically disordered proteins. *Arch. Biochem. Biophys.* **2017**, *628*, 57–70.
- (5) Schneider, R.; Huang, J.; Yao, M.; Communie, G.; Ozenne, V.; Mollica, L.; Salmon, L.; Ringkjøbing Jensen, M.; Blackledge, M. Towards a robust description of intrinsic protein disorder using nuclear magnetic resonance spectroscopy. *Mol. BioSyst.* **2012**, *8* (1), 58–68.
- (6) Pramanik, U.; Chakraborty, S.; Bhattacharyya, K.; Mukherjee, S. An intrinsically disordered protein in F127 hydrogel: Fluorescence correlation spectroscopy and structural diversity of beta casein. *J. Phys. Chem. Lett.* **2021**, *12*, 138105.
- (7) Zosel, F.; Haenni, D.; Soranno, A.; Nettels, D.; Schuler, B. Combining short- and long-range fluorescence reporters with simulations to explore the intramolecular dynamics of an intrinsically disordered protein. *J. Chem. Phys.* **2017**, *147* (15), 152708.
- (8) Kodera, N.; Ando, T. Visualization of intrinsically disordered proteins by high-speed atomic force microscopy. *Curr. Opin. Struct. Biol.* **2022**, *72*, 260–266.
- (9) Kodera, N.; Noshiro, D.; Dora, S. K.; Mori, T.; Habchi, J.; Blocquel, D.; Gruet, A.; Dosnon, M.; Salladini, E.; Bignon, C.; et al. Structural and dynamics analysis of intrinsically disordered proteins by high-speed atomic force microscopy. *Nat. Nanotechnol.* **2021**, *16* (2), 181–189.
- (10) Huang, F.; Rajagopalan, S.; Settanni, G.; Marsh, R. J.; Armoogum, D. A.; Nicolaou, N.; Bain, A. J.; Lerner, E.; Haas, E.; Ying, L.; et al. Multiple conformations of full-length p53 detected with single-molecule fluorescence resonance energy transfer. *Proc. Natl. Acad. Sci. U.S.A.* **2009**, *106* (49), 20758–20763.
- (11) Okamoto, K.; Sako, Y. Single-molecule Förster resonance energy transfer measurement reveals the dynamic partially ordered structure of the epidermal growth factor receptor C-tail domain. *J. Phys. Chem. B* **2019**, *123* (3), 571–581.
- (12) Mukhopadhyay, S.; Krishnan, R.; Lemke, E. A.; Lindquist, S.; Deniz, A. A. A natively unfolded yeast prion monomer adopts an ensemble of collapsed and rapidly fluctuating structures. *Proc. Natl. Acad. Sci. U.S.A.* **2007**, *104* (8), 2649–2654.
- (13) Japrun, D.; Dogan, J.; Freedman, K. J.; Nadzeyka, A.; Bauerdick, S.; Albrecht, T.; Kim, M. J.; Jemth, P.; Edell, J. B. Single-molecule studies of intrinsically disordered proteins using solid-state nanoprobes. *Anal. Chem.* **2013**, *85* (4), 2449–2456.
- (14) Oh, S.; Lee, M. K.; Chi, S. W. Single-molecule analysis of interaction between p53TAD and MDM2 using aerolysin nanopores. *Chem. Sci.* **2021**, *12* (16), 5883–5891.
- (15) He, G.; Li, J.; Ci, H.; Qi, C.; Guo, X. Direct measurement of single-molecule DNA hybridization dynamics with single-base resolution. *Angew. Chem., Int. Ed.* **2016**, *128* (31), 9182–9186.
- (16) Li, J.; He, G.; Hiroshi, U.; Liu, W.; Noji, H.; Qi, C.; Guo, X. Direct measurement of single-molecule adenosine triphosphatase hydrolysis dynamics. *ACS Nano* **2017**, *11* (12), 12789–12795.
- (17) Liu, W.; Li, J.; Xu, Y.; Yin, D.; Zhu, X.; Fu, H.; Su, X.; Guo, X. Complete mapping of DNA-protein interactions at the single-molecule level. *Adv. Sci.* **2021**, *8* (23), 2101383.
- (18) Yang, Z.; Qi, C.; Liu, W.; Yin, D.; Yu, L.; Li, L.; Guo, X. Revealing conformational transition dynamics of photosynthetic proteins in single-molecule electrical circuits. *J. Phys. Chem. Lett.* **2021**, *12* (15), 3853–3859.
- (19) Fuller, C. W.; Padayatti, P. S.; Abderrahim, H.; Adamiak, L.; Alagar, N.; Ananthapadmanabhan, N.; Baek, J.; Chinni, S.; Choi, C.; Delaney, K. J.; et al. Molecular electronics sensors on a scalable semiconductor chip: A platform for single-molecule measurement of binding kinetics and enzyme activity. *Proc. Natl. Acad. Sci. U.S.A.* **2022**, *119* (5), No. e2112812119.
- (20) Choi, Y.; Moody, I. S.; Sims, P. C.; Hunt, S. R.; Corso, B. L.; Perez, I.; Weiss, G. A.; Collins, P. G. Single-molecule lysozyme dynamics monitored by an electronic circuit. *Science* **2012**, *335* (6066), 319–324.
- (21) Choi, Y.; Olsen, T. J.; Sims, P. C.; Moody, I. S.; Corso, B. L.; Dang, M. N.; Weiss, G. A.; Collins, P. G. Dissecting single-molecule signal transduction in carbon nanotube circuits with protein engineering. *Nano Lett.* **2013**, *13* (2), 625–631.
- (22) Turvey, M. W.; Gabriel, K. N.; Lee, W.; Taulbee, J. J.; Kim, J. K.; Chen, S.; Lau, C. J.; Kattan, R. E.; Pham, J. T.; Majumdar, S.; et al. Single-molecule Taq DNA polymerase dynamics. *Sci. Adv.* **2022**, *8* (10), No. eabl3522.
- (23) Akhterov, M. V.; Choi, Y.; Olsen, T. J.; Sims, P. C.; Iftikhar, M.; Gul, O. T.; Corso, B. L.; Weiss, G. A.; Collins, P. G. Observing lysozyme's closing and opening motions by high-resolution single-molecule enzymology. *ACS Chem. Biol.* **2015**, *10* (6), 1495–1501.
- (24) Zhang, B.; Deng, H.; Mukherjee, S.; Song, W.; Wang, X.; Lindsay, S. Engineering an enzyme for direct electrical monitoring of activity. *ACS Nano* **2020**, *14* (2), 1360–1368.
- (25) Zhang, B.; Ryan, E.; Wang, X.; Lindsay, S. Probing bioelectronic connections using streptavidin molecules with modified valency. *J. Am. Chem. Soc.* **2021**, *143* (37), 15139–15144.
- (26) Patolsky, F.; Zheng, G.; Hayden, O.; Lakadamyali, M.; Zhuang, X.; Lieber, C. M. Electrical detection of single viruses. *Proc. Natl. Acad. Sci. U.S.A.* **2004**, *101* (39), 14017–14022.
- (27) Wang, J.; Shen, F.; Wang, Z.; He, G.; Qin, J.; Cheng, N.; Yao, M.; Li, L.; Guo, X. Point Decoration of Silicon Nanowires: An Approach Toward Single-Molecule Electrical Detection. *Angew. Chem., Int. Ed.* **2014**, *126* (20), 5138–5143.
- (28) Liu, W.; Chen, L.; Yin, D.; Yang, Z.; Feng, J.; Sun, Q.; Lai, L.; Guo, X. Visualizing single-molecule conformational transition and binding dynamics of intrinsically disordered proteins. *Nat. Commun.* **2023**, *14* (1), 5203.
- (29) Bode, A. M.; Dong, Z. Post-translational modification of p53 in tumorigenesis. *Nat. Rev. Cancer* **2004**, *4* (10), 793–805.
- (30) Vousden, K. H.; Lane, D. P. p53 in health and disease. *Nat. Rev. Mol. Cell Biol.* **2007**, *8* (4), 275–283.
- (31) Vousden, K. H.; Prives, C. Blinded by the light: the growing complexity of p53. *Cell* **2009**, *137* (3), 413–431.
- (32) Wells, M.; Tidow, H.; Rutherford, T. J.; Markwick, P.; Jensen, M. R.; Mylonas, E.; Svergun, D. I.; Blackledge, M.; Fersht, A. R. Structure of tumor suppressor p53 and its intrinsically disordered N-terminal transactivation domain. *Proc. Natl. Acad. Sci. U. S. A.* **2008**, *105* (15), 5762–5767.

- (33) Ruan, H.; Sun, Q.; Zhang, W.; Liu, Y.; Lai, L. Targeting intrinsically disordered proteins at the edge of chaos. *Drug Discovery Today* **2019**, *24* (1), 217–227.
- (34) Boehr, D. D.; Nussinov, R.; Wright, P. E. The role of dynamic conformational ensembles in biomolecular recognition. *Nat. Chem. Biol.* **2009**, *5* (11), 789–796.
- (35) Csermely, P.; Palotai, R.; Nussinov, R. Induced fit, conformational selection and independent dynamic segments: an extended view of binding events. *Trends Biochem. Sci.* **2010**, *35* (10), 539–546.
- (36) Yin, D.; Li, J.; Feng, J.; Liu, W.; Yang, Z.; Li, S.; Li, M.; Li, L.; Guo, X. Direct mechano-sliding transfer of chemical vapor deposition grown silicon nanowires for nanoscale electronic devices. *J. Mater. Chem. C* **2022**, *10* (2), 469–475.
- (37) Ruan, H.; Yu, C.; Niu, X.; Zhang, W.; Liu, H.; Chen, L.; Xiong, R.; Sun, Q.; Jin, C.; Liu, Y.; et al. Computational strategy for intrinsically disordered protein ligand design leads to the discovery of p53 transactivation domain I binding compounds that activate the p53 pathway. *Chem. Sci.* **2021**, *12* (8), 3004–3016.
- (38) McKinney, S. A.; Joo, C.; Ha, T. Analysis of single-molecule FRET trajectories using hidden Markov modeling. *Biophys. J.* **2006**, *91* (5), 1941–1951.
- (39) Micsónai, A.; Moussong, E.; Wien, F.; Boros, E.; Vadász, H.; Murvai, N.; Lee, Y.-H.; Molnár, T.; Réfrégiers, M.; Goto, Y.; et al. BeStSel: webserver for secondary structure and fold prediction for protein CD spectroscopy. *Nucleic Acids Res.* **2022**, *50* (W1), W90–W98.
- (40) Wishart, D. S.; Sykes, B. D. The ^{13}C chemical-shift index: a simple method for the identification of protein secondary structure using ^{13}C chemical-shift data. *J. Biomol. NMR* **1994**, *4*, 171–180.
- (41) Anada, C.; Ikeda, K.; Egawa, A.; Fujiwara, T.; Nakao, H.; Nakano, M. Temperature- and composition-dependent conformational transitions of amphipathic peptide-phospholipid nanodiscs. *J. Colloid Interface Sci.* **2021**, *588*, 522–530.
- (42) Schlitter, J.; Engels, M.; Krüger, P. Targeted molecular dynamics: a new approach for searching pathways of conformational transitions. *J. Mol. Graphics* **1994**, *12* (2), 84–89.
- (43) Dyson, H. J.; Wright, P. E. Coupling of folding and binding for unstructured proteins. *Curr. Opin. Struct. Biol.* **2002**, *12* (1), 54–60.
- (44) Kussie, P. H.; Gorina, S.; Marechal, V.; Elenbaas, B.; Moreau, J.; Levine, A. J.; Pavletich, N. P. Structure of the MDM2 oncoprotein bound to the p53 tumor suppressor transactivation domain. *Science* **1996**, *274* (5289), 948–953.
- (45) Chène, P. Inhibiting the p53-MDM2 interaction: an important target for cancer therapy. *Nat. Rev. Cancer* **2003**, *3* (2), 102–109.
- (46) Moll, U. M.; Petrenko, O. The MDM2-p53 interaction. *Mol. Cancer Res.* **2003**, *1* (14), 1001–1008.
- (47) Haupt, Y.; Maya, R.; Kazaz, A.; Oren, M. Mdm2 promotes the rapid degradation of p53. *Nature* **1997**, *387* (6630), 296–299.
- (48) Kubbutat, M. H.; Jones, S. N.; Vousden, K. H. Regulation of p53 stability by Mdm2. *Nature* **1997**, *387* (6630), 299–303.
- (49) Nomura, K.; Klejnot, M.; Kowalczyk, D.; Hock, A. K.; Sibbet, G. J.; Vousden, K. H.; Huang, D. T. Structural analysis of MDM2 RING separates degradation from regulation of p53 transcription activity. *Nat. Struct. Mol. Biol.* **2017**, *24* (7), 578–587.
- (50) Koshland, D. E., Jr. Application of a theory of enzyme specificity to protein synthesis. *Proc. Natl. Acad. Sci. U.S.A.* **1958**, *44* (2), 98–104.
- (51) Borchers, W.; Theillet, F.-X.; Katzer, A.; Finzel, A.; Mishall, K. M.; Powell, A. T.; Wu, H.; Manieri, W.; Dieterich, C.; Selenko, P.; et al. Disorder and residual helicity alter p53-Mdm2 binding affinity and signaling in cells. *Nat. Chem. Biol.* **2014**, *10* (12), 1000–1002.
- (52) Feng, H.; Jenkins, L. M. M.; Durell, S. R.; Hayashi, R.; Mazur, S. J.; Cherry, S.; Tropea, J. E.; Miller, M.; Wlodawer, A.; Appella, E.; et al. Structural basis for p300 Taz2-p53 TAD1 binding and modulation by phosphorylation. *Struct. Bonding (Berlin)* **2009**, *17* (2), 202–210.
- (53) Van Der Spoel, D.; Lindahl, E.; Hess, B.; Groenhof, G.; Mark, A. E.; Berendsen, H. J. GROMACS: fast, flexible, and free. *J. Comput. Chem.* **2005**, *26* (16), 1701–1718.
- (54) Piana, S.; Donchev, A. G.; Robustelli, P.; Shaw, D. E. Water dispersion interactions strongly influence simulated structural properties of disordered protein states. *J. Phys. Chem. B* **2015**, *119* (16), 5113–5123.
- (55) Wu, H. N.; Jiang, F.; Wu, Y. D. Significantly improved protein folding thermodynamics using a dispersion-corrected water model and a new residue-specific force field. *J. Phys. Chem. Lett.* **2017**, *8* (14), 3199–3205.
- (56) Chong, S. H.; Chatterjee, P.; Ham, S. Computer simulations of intrinsically disordered proteins. *Annu. Rev. Mater. Res.* **2017**, *68*, 117–134.
- (57) Greenfield, N. Using circular dichroism spectra to estimate protein secondary structure. *Nat. Protoc.* **2006**, *1* (6), 2876–2890.
- (58) Kelly, S. M.; Jess, T. J.; Price, N. C. How to study proteins by circular dichroism. *Biochim. Biophys. Acta* **2005**, *1751* (2), 119–139.